LAWRENCE
LIVERMORE
NATIONAL
LABORATORY

LLNL-JRNL-807382

Quantification of the modulus of dentine apatite nanoparticles by in situ diffraction and pressurization reveals stiffening upon carbonate removal

J. B. Forien, J. Uzuhashi, T. Ohkubo, L. Luo, H. P. Schwarcz, A. C. Deymier, C. Krywka, C. Fleck, P. Zaslansky

March 18, 2020

Acta Biomaterialia

Disclaimer

X-ray diffraction and *in situ* pressurization of dentine apatite nanocrystals quantifies modulus stiffening upon carbonate removal

Jean-Baptiste Forien[1], Jun Uzuhashi[2], Tadakatsu Ohkubo[2], Kazuhiro Hono[2], Lucy Luo[3], Henry P. Schwarcz[3], Alix C. Deymier[4], Christina Krywka[5], Claudia Fleck[6], Paul Zaslansky[7]

[1]Lawrence Livermore National Laboratory, 94550 Livermore, United States of America
[2]National Institute for Materials Science, 305-0047 Tsukuba, Japan
[3]McMaster University, School of Geography and Earth Sciences, ON L8S 4L8 Hamilton, Canada
[4]University of Connecticut Health Center, CT 06030 Farmington, United States of America
[5]Helmholtz-Zentrum Geesthacht, 21502 Geesthacht, Germany
[6]Technische Universität Berlin, Materials Science & Engineering, 10623 Berlin, Germany
[7]Charité – Universitätsmedizin Berlin, Restorative and Preventive Dentistry, 14497 Berlin, Germany

Graphical Abstract

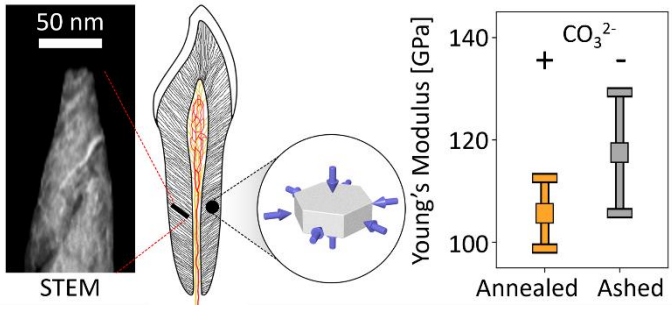

Abstract

Bone-like materials comprise carbonated-hydroxyapatite nanocrystals (c-Ap) embedding a fibrillar collagen matrix. The mineral particles stiffen the nanocomposite by tight attachment to the protein fibrils creating a high strength and toughness material. The nanometer dimensions of c-Ap crystals make it very challenging to measure their mechanical properties. Mineral in bony tissues such as dentine contains 2~6 wt.% carbonate with possibly different elastic properties as compared with crystalline hydroxyapatite. Here we determine strain in biogenic apatite nanocrystals by directly measuring atomic deformation in pig dentine before and after removing carbonate. Transmission electron microscopy revealed the platy 3D morphology while atom probe tomography demonstrated carbon situated inside the crystals. High-energy X-ray diffraction in combination with *in situ* hydrostatic pressurization quantified reversible c-Ap deformations. Crystal strains differed between annealed and ashed (decarbonated) samples, following 1 or 10 hours heating at 250°C or 550°C respectively. Measured bulk moduli-(K) and a-/c-lattice deformation ratios-(η) were used to generate synthetic K and η identifying the most likely elastic constants C_{33} and C_{13} for c-Ap. These are then used to calculate the nanoparticle elastic moduli. For ashed samples, we find an average E_{11}=107GPa and E_{33}=128GPa corresponding to ~5% and ~17% stiffening of the a-/c-axes of the nanocrystals as compared with the biogenic nanocrystals in annealed samples. Ashed

samples exhibit ~10% lower Poisson's ratios as compared with the 0.25~0.36 range of carbonated apatite. Carbonate in c-Ap may therefore serve for tuning local deformability within bony tissues.

Keywords: XRD, BF/DF TEM, STEM, Atom Probe Tomography - APT, Carbonated Apatite, Hydrostatic pressure, bony nanocomposite, Bulk modulus, Young's modulus, Poisson's ratio

1. Introduction

Mineralized collagen fibrils are the solution that evolution came up with, for construction of the majority of calcified rigid body parts in mammals and most other vertebrates [1]. The bony multipurpose biogenic nano-composite is found in many skeletal elements including bones, mineralized tendons, antlers and tooth dentine. The organic component is made of protein fibrils (collagen type I, ~30 vol.%) that are reinforced with mineral nanoparticles of carbonated apatite crystals (c-Ap, 50 vol.%), and both components are tightly attached to water and minor organic additives, comprising the remaining biocomposite volume. Already in the growing tissue, the *c*-axes of the mineral crystals are approximately aligned with the long axis of the collagen protein [2,3]. Fig. 1 shows a schematic representation of the bony constituents [4–6], illustrating how the nano-scale ingredients combine into larger (submicron) assemblies of mineralized collagen fibrils. By mesoscale ordering (e.g. into rotated plywood motifs), larger microstructures such as lamellae emerge, and these combine into even larger typical architectures such as osteons, trabeculae, mantle dentine [7]. Although these tissues may serve as reservoirs of Ca ions, it is the stiffness, enhanced by the c-Ap bioceramic, that makes mineralized collagen fibres so central for locomotion and defence among vertebrates [8]. Notably, the nanocomposite is well suited to elastically and reversibly sustain naturally encountered compression, tension and torsion loading.

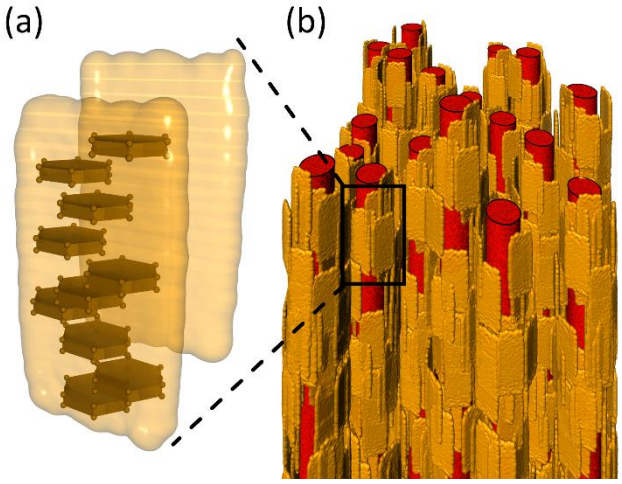

Fig. 1: Schematic representation of mineralized collagen fibrils. *(a) c-Ap crystals with hexagonal unit cells (illustrated in brown) adhere to other crystals to form clusters of mineral (polycrystalline) that attach and partially wrap around collagen fibrils, creating (b) bundles of mineralized fibrils forming a composite. The collagen fibrils (marked red) are made of bundles of triple helix molecules. Note that the schematic composition is not drawn to scale.*

The elastic properties of c-Ap based biocomposites have been the subject of investigations for many decades. Stiffness of the bony tissue was found to increase as a function of mineral content [1]. Fibril orientations also play an important stiffening role, exhibiting higher stiffness along the fibril axis demonstrated, e.g. for lamellar bone [9] or narwhal dentine [10]. The fibrils and crystals contribute importantly but differently to the task of resisting deformation due to external loads: whereas the collagen fibrils are best suited for sustaining tension, the mineral nanoparticles are the main source of compression resistance. Through the tight and exceptionally strong bond between the fibrils and the c-Ap particles [11,12] the composite exhibits both strength and toughness that outperform the contributions of each ingredient separately. Isolated collagen fibrils directly measured in tension, yielded Young's modulus values ranging from 0.2 to 0.8 GPa [13–15]. Reports of tensile measurements performed on mineralized collagen fibrils [16] demonstrated that the apatite crystals also contribute significantly to increasing axial tensile stiffness, thus sustaining high loads also in tension, due to their exceptional mechanical properties [17,18]. Indeed, the elastic properties of the crystals are of paramount importance for the mechanical competence of bony tissues.

However so far, it has not been possible to directly measure the mechanical properties of the nanoparticles themselves, and specifically the crystals that comprise them. In fact, the elastic properties of c-Ap nanocrystals are widely assumed to be identical to those of geological apatites, where larger samples make it easier to experimentally determine the deformation response [19]. Work performed over much of the 20th century has reported the properties of different geological samples of fluoro-, chloro- and hydroxyapatite using a variety of methods. These include measurements using ultrasonic pulsed waves [20–23], high-pressure [24,25], and X-ray diffraction under compression [26–29]. Elastic moduli of synthetic and biological apatites have been estimated using bending tests [30], indentation experiments [31–37], and direct compression testing [38]. None of these, however, could directly measure the properties of the mineral crystals in bone tissues. To overcome the technical limitations of performing mechanical measurements on such tiny particles, computer simulations have been used employing various sorts of modelling such as force field [39–41], *ab initio* [42–45] and density-functional theory [46–48]. All the above provided bounds or estimates of what the properties of the c-Ap are likely to be, with reports of Young's moduli spanning 54-147 GPa. Recently, Forien *et al.* [49] reported measurements by *in situ* hydrostatic pressurization of c-Ap nanoparticles embedded within samples of natural dentine. Direct comparisons of these experimental deformation results and simulations reported by Menéndez-Proupin *et al.* [40] showed that pristine c-Ap has lower elastic moduli, as compared to geological apatites.

Both biological and geological apatites contain carbonate ions (CO_3^{2-}) in the crystal lattice. Carbonate content may reach ~6 wt.% in bone [19]; a range of ~4.5-5.6 wt.% has been suggested for dentine [19,50] although recently, for large numbers of teeth, only 2~2.5% were reported [51]. Carbonate substitutions may in principle occupy both phosphate and hydroxide lattice sites [52], better known as B- and A-type substitutions, respectively. These substitutions have opposite effects on the lattice parameters: whereas increasing B-type substitution results in apatite crystals exhibiting a shortening and lengthening of the *a*- and *c*-lattice parameters, respectively, A-type substitutions cause expansion of *a*- and contraction of the *c*-axis dimensions [19]. There have been many reports that B-type substitutions are more prevalent, but these may well be attributed to overlapping bands in the vibrational spectroscopy measurements [53]. Alternative findings suggest that there may be similar prevalence of A- and B-type substitutions in both bone and dentine c-Ap [53,54]. Increasing carbonate content in synthetic

precipitated c-Ap powder decreases its chemical stability and increases its solubility [55]. Other chemical substitution and vacancies in c-Ap induce further changes in the crystal lattice, which may also affect mechanical rigidity. As previously reported elsewhere [39,49] stiffness in c-Ap can be expressed using fundamental parameters describing the relations between stress and strain, known as the elastic constants of the hexagonal material stiffness tensor (C_{ij}). Simulations using molecular dynamics (MD) models and employing density functional theory (DFT) to estimate c-Ap surface energy predicted a decrease in the stiffness of two of the elastic constants (C_{13}, C_{33}) as a function of increasing CO_3^{2-} content [39]. The effects of carbonate variations on the elastic moduli (E_{11}, E_{33}) of crystals within natural, mineralized collagen fibres have not yet been determined. It is plausible that, similar to increasing carbonate content in synthetic apatite [39], the carbonate (CO_3^{2-}) content of natural c-Ap in dentine has a softening influence on the modulus of biogenic crystals. In previous work, Forien *et al.* [49], did not address possible differences between the fundamental independent elastic constants of the different samples, nor did they directly demonstrate a link between changes in carbonate content in c-Ap and changes in stiffness. Yet, exposing bony materials to heat treatment can change the carbonate content in the mineral phase. Indeed, several studies have reported a decrease in CO_3^{2-} as a function of exposure to temperatures exceeding 500 °C, using both thermogravimetric and infrared spectroscopy methods. This has been shown for dentine and enamel samples [51,56], as well as for deer antler and whale tympanic bulla [57], sheep bone [58], bovine bone [59] and also precipitated human tooth enamel c-Ap powder [60]. It is however not known how such compositional changes may affect the c-Ap elastic properties.

In the present work, we exploit heat treatment as a means to remove CO_3^{2-} from c-Ap nanocrystals to measure the effects of decarbonation on the mechanical deformation of the nanocrystals in pig dentine. We directly determine both bulk modulus (K) and a- and c-lattice deformation ratios (η) of the apatite by *in situ* high-energy X-ray diffraction on annealed [11] and ashed dentine samples. In the latter, carbonate is removed by heating. For the c-Ap hexagonal crystal system of apatite, we identify all combinations of sets of the four elastic constants C_{11}, C_{12}, C_{13}, C_{33}, that yield K and η close to the results that we obtain experimentally. Then, we use synthetic distributions of these constants to identify the most probable values relevant for biogenic apatite, considering our own measured K and η. These results reveal the elastic constants C_{13}, C_{33} of annealed c-Ap and of carbonate-free c-Ap particles. Based on these constants we derive refined mineral particle moduli (E_{11}, E_{33}) and the corresponding orthogonal Poisson's ratios (ν_{basal}, ν_{prism}). High-resolution transmission electron microscopy (TEM) and atom probe tomography (APT) provided structural explanations supporting our mechanical experiments to better understand effects of carbonate removal from biogenic c-Ap nanoparticles in mineralized collagen fibrils of tooth dentine.

2. Materials and methods

2.1 Sample preparation

Jaws from slaughtered adult sows (20+ months old) were obtained from an abattoir, and the anterior teeth were extracted and pooled for storage at 4 °C in a refrigerator in chloramine-T 0.5% solution. A total of ten permanent-dentition front teeth were used as follows. For structural characterization, three roots were dedicated to scanning transmission electron microscopy (STEM) and APT. An additional root was used for bright- and dark-field TEM measurements of crystal dimensions. The remaining six teeth were used for X-ray diffraction measurements. Three of these were previously

measured wet (in a so-called pristine state) as reported in our earlier study [49]. Those samples were used to produce multiple slices (n = 17) that were heat treated under ambient (oxidizing) conditions at 250 °C for 1 hour, to destroy collagen and to release residual stresses on the crystals [11-12]. The other three roots were cut out of hydrated pig teeth and were ashed by heat treatment at 550 °C for 10 hours. In this manner, 2 groups of heat-treated samples were created following short exposure to a low temperature, addressed as "annealed" samples, and following long exposure to a high temperature, named "ashed". These treatments led to the usual colour changes, as previously reported [59,61]: the annealed dentine samples appeared charred with variable degrees of dark brown; the ashed samples became visibly dark grey with patches of white. Each of the annealed and ashed samples was mounted dry in a pressurization chamber, hydrated and then hydrostatically compressed for *in situ* diffraction analysis, as described below.

All samples used for structural characterization by TEM/STEM/APT were extracted from pristine intertubular pig dentine. Root dentine was sliced using water-cooled diamond saws. Following air drying, the samples were either thinned, dimpled and ion-milled in a cryo-ion-mill for TEM, or they were focused-ion beam (FIB) SEM milled for the STEM and APT analyses. The FIB-SEM was also used to mill an ashed sample and to create the necessary conical nano pillar shapes required for APT analysis. Intertubular root dentine was extracted from material located between tubules so that pillars could be created with ~100 nm diameter at the base.

2.2 X-ray *in situ* pressurization and diffraction experiments

X-ray synchrotron measurements were performed during two different experimental runs at the P07 High Energy Materials Science beamline (HEMS) operated by Helmholtz Zentrum Geesthacht (HZG) at the PETRA III storage ring (DESY, Hamburg, Germany). Energies of 53.7 and 60 keV, and a beam-size of 1 x 1 mm^2 were used to project diffraction patterns on a 2048 x 2048 pixel Perkin Elmer 1621 flat panel detector. In the two experiments, the detector was positioned 1.39 m and 1.52 m, respectively, downstream of a custom-built hydrostatic pressure chamber and diffraction patterns were collected with 6 s and 10 s exposure times, respectively. The dedicated chamber capable of sustaining hydrostatic pressure of up to 400 MPa, contained entry and exit diamond windows in near proximity to the sample to allow passage of the X-rays, as previously described [49,62,63]. Each sample (Fig. 2a) was mounted in the beam path and the chamber was sealed in preparation for hydration and pressurization (Fig. 2b). Diffraction patterns were collected on the dry samples (data not shown) after which water was injected into the system while removing air. Each sample was allowed to equilibrate in the hydrated chamber for 10 minutes under minimal water pressure (5 MPa, resulting in ~0.002 Å relaxation and *c*-lattice expansion, as compared with the dry state). Thereafter multiple (n = 11) diffraction patterns were recorded at each hydrostatic increment, followed by stepwise increments in pressure to 200 and to 400 MPa for the annealed samples, but with smaller incremental steps of 100, 200, 300 and 350 MPa for the ashed samples. Additional unloaded diffraction patterns were collected immediately after load release and also following an additional 10 min waiting time.

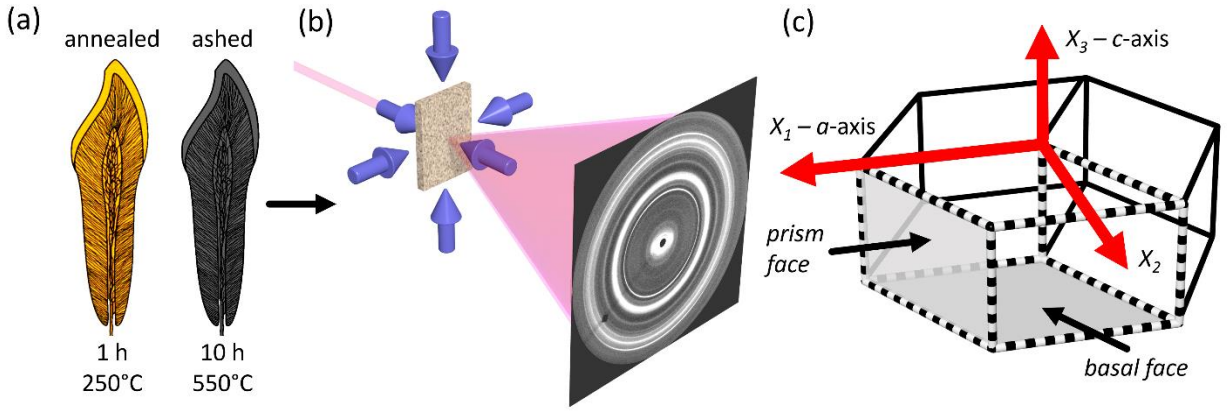

Fig. 2: Experimental design. *(a) Schematic representation of samples that were heat treated (b). Following hydration, each sample was hydraulically compressed in water while measuring diffraction patterns in pre-loaded, pressurized and unloaded states. (c) Diffraction peaks were used to track the interplanar a- and c-lattice spacings under different states of hydration and load. The orthogonal axes of the hexagonal c-Ap crystals are defined using the illustrated Cartesian coordinate system: X_1 corresponds to the crystalline a-axis and is oriented parallel to the basal face, X_3 is oriented along the c-axis, perpendicular to the basal face. The X_2-axis lies in the basal hexagon plane, perpendicular to both the X_1- and X_3-axes.*

2.3 XRD data analysis

Calibration of the sample-detector distance as well as analysis of the diffraction pattern peak positions were performed using the XRDUA analysis kit (v.6432) [64]. Camera tilt and rotation angle, sample-to-detector distance, and x-/y-pixel centre parameters were refined based on LaB6 powder standards. Entire azimuthal integrations of the (002) and (310) Debye-Scherrer rings yielded peaks that were used to calculate the apatite *c*- and *a*- axis lattice parameters. The resulting 1D-data (intensity versus 2-theta) were normalized with respect to "empty beam" measurements obtained from diffraction patterns of water in the chamber, pressurized to levels corresponding to the sample loading states. Thus, peak positions were tracked in the normalized intensity profiles of apatite, accounting for the effects of passage of the X-ray beam through water. Custom code was used for peak fitting of a Voigt function and subtracting a 1st order polynomial background for the (002) reflection, while employing a combination of a Voigt and two Gaussian functions with a 1st order polynomial background for fitting the (310) reflection. Peak refinement was performed using Python 2.7 [65] employing the Lmfit package [66]. Resulting fits of repeated measurements (n = 11 at each given pressure for each sample) were averaged and used to determine the mean *a*- and *c*-lattice parameters (d-spacing) of the apatite nanocrystals. Strain along these main crystallographic axes, defined as $\varepsilon_1 = \Delta a/a$ and $\varepsilon_3 = \Delta c/c$, was determined with respect to the initial reference measurements performed following hydration for 10 min (see supplementary Fig. S1). The measurements of unloaded samples were used for comparison with the initial, unloaded state to identify changes in the lattice spacings after load. Measurements revealed that strains either recovered fully (data not shown) or showed some minimal (~0.0015 Å) relaxation due to continuous hydration. Comparison of repeated measurements in the unloaded states demonstrated that uncertainty was ±0.00017 Å for fits to the (310) peak and ±0.00002 Å for fits to the (002) peak. The estimated error in our strain determinations is therefore less than 0.01%.

2.4 Elastic constants determination

Analysis was performed assuming a hexagonal crystal system (Fig. 2c), as has been previously described (see e.g. [67–69]). Briefly, the stiffness matrix is defined by five independent elastic constants, C_{11}, C_{12}, C_{12}, C_{33} and C_{44} related by the stiffness tensor:

$$C = \begin{bmatrix} C_{11} & C_{12} & C_{13} & 0 & 0 & 0 \\ C_{12} & C_{11} & C_{13} & 0 & 0 & 0 \\ C_{13} & C_{13} & C_{33} & 0 & 0 & 0 \\ 0 & 0 & 0 & C_{44} & 0 & 0 \\ 0 & 0 & 0 & 0 & C_{44} & 0 \\ 0 & 0 & 0 & 0 & 0 & {(C_{11} - C_{12})}/{2} \end{bmatrix} \quad (1)$$

from which the bulk modulus (K) can be derived as:

$$K = \frac{\sigma}{({\Delta V}/{V})} = \frac{[(C_{11}+C_{12})C_{33}]-2{C_{13}}^2}{C_{11}+C_{12}+2C_{33}-4C_{13}} \quad (2)$$

Further, η, the ratio of the *a*- and *c-Ap* crystal lattice strains (ε_1 and ε_3 respectively) is defined as:

$$\eta = \frac{\varepsilon_1}{\varepsilon_3} = \frac{C_{33}-C_{13}}{C_{11}+C_{12}-2C_{13}} \quad (3)$$

Building on our previous work [49], the measured data were used to generate distributions of all possible elastic constant combinations, where synthetic C_{ij} were compared to physical measurements of K_{meas} and η_{meas} (subscript *meas* for measured data) based on the relations in eqs. (2), (3). To achieve this, sets of all possible combinations of the elastic constants C_{ij} were generated, each ranging from 0 to 200 GPa (6,250,000 combinations, each constant varied by increments of 4 GPa to reduce excessive computation times). From each combination of those synthetic C_{11}, C_{12}, C_{13}, C_{33}, the corresponding values of K_{syn} and η_{syn} (subscript *syn* for synthetically generated data) were calculated with a constraint that only positive values were considered. Example resulting 2D histograms of K_{syn} and η_{syn} are shown in supplementary Fig. S2. Each pair K_{syn} and η_{syn} was then compared to all measured K_{meas} and η_{meas} data obtained experimentally by our XRD experiments. All discrepancy values were calculated according to:

$$discrepancy = \left[\left(\eta_{syn}/\eta_{meas}\right) - 1\right]^2 + \left[\left(K_{syn}/K_{meas}\right) - 1\right]^2 \quad (4)$$

where *discrepancy* is the sum of the normalized square differences between the synthetic and measured parameters: K_{syn} versus K_{meas} and η_{syn} versus η_{meas}. From the synthetically generated distributions of K_{syn} and η_{syn}, a majority (95%) of the data was discarded retaining only 5% of pairs of parameters with the lowest *discrepancy*. The combinations of elastic constants C_{11}, C_{12}, C_{13}, C_{33} corresponding to the most likely constants were further explored to identify the maximum occurrence of each of the elastic stiffness constants, by imposing additional boundary conditions. The first empirical assumption made was that C_{33} > 100 GPa and C_{13} < 100 GPa, based on previously published experiments. With these constraints in place, we observed the emergence of a clear peak in the distribution of C_{13} when limiting K to span 'realistic' bulk moduli, within the range of 80 to 90 GPa. This range was chosen based on our own experimental results (mean 85 GPa for both annealed and ashed samples) as well as on previously reported K values in the literature (summarized in [49], Table 1). Once probable values of C_{13} were determined separately for the annealed and ashed samples, it was possible to determine the maximum occurrence of C_{33} that best

corresponded to our measured K_{meas} and η_{meas} by slightly varying C_{13} (arbitrarily chosen as ±2 GPa to match our bin sizes). The two other constant distributions C_{11} and C_{12} did not converge, exhibiting similar probabilities for all values previously reported in the literature, spanning ranges of 118-137 GPa and 31-53 GPa for C_{11} and C_{12} respectively. Since no better estimates of these parameters was possible experimentally, we examined values proposed for different simulations reported in the literature [22,39,40] in addition to values derived from molecular dynamic simulations based on our K_{meas} and η_{meas}. The resulting C_{ij} sets were then used to calculate textbook solutions to the elastic moduli E_{11}, E_{33}, as well as the average Poisson's ratios v_{basal}, v_{prism}, derived from the deformation in the basal and prism planes with respect to the orthogonal *c*- and *a*-axes (see e.g. [49,69]), according to:

$$E_{11} = E_{22} = 1/S_{11}$$
$$E_{33} = 1/S_{33} \quad (5)$$

$$\upsilon_{prism} = -\frac{[\varepsilon_2+\varepsilon_3]}{2\varepsilon_1} = -\frac{[\varepsilon_1+\varepsilon_3]}{2\varepsilon_1} = -\frac{[S_{12}+S_{13}]}{2S_{11}}$$

$$\upsilon_{basal} = -\frac{[\varepsilon_2+\varepsilon_1]}{2\varepsilon_3} = -\frac{S_{13}}{S_{33}} \quad (6)$$

where

$$S_{11} = \frac{C_{33}C_{11}-{C_{13}}^2}{[C_{33}(C_{11}+C_{12})-2{C_{13}}^2](C_{11}-C_{12})}$$

$$S_{33} = \frac{C_{11}+C_{12}}{C_{33}(C_{11}+C_{12})-2{C_{13}}^2} \quad (7)$$

A schematic illustration of the computation steps used to determine the constants and the elastic properties of apatite is provided in Fig. 3.

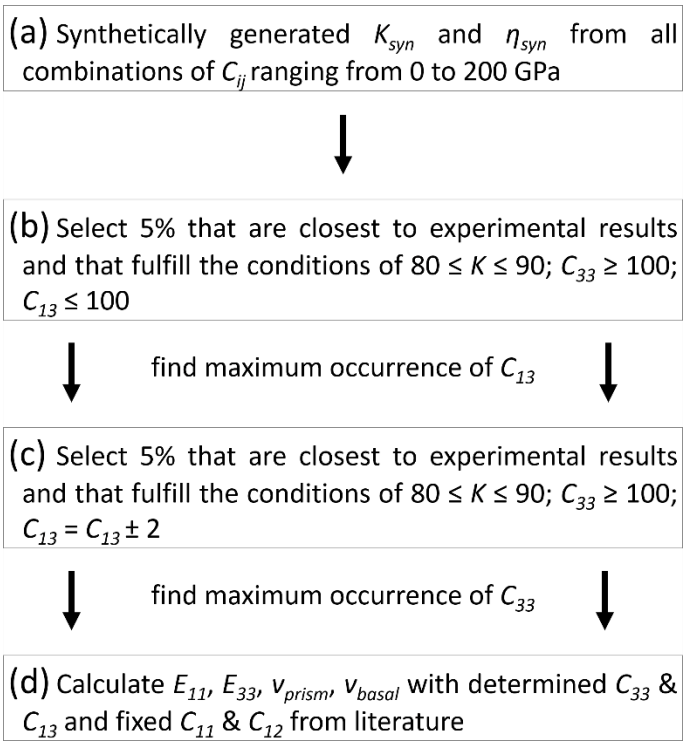

Fig. 3: Schematic representation of the steps required to derive the Young's moduli E_{11} and E_{33}. *(a) Multiple K_{syn} and η_{syn} values were generated from all combinations of C_{ij}, negative values are discarded. (b) Rejection of 95% of the generated K_{syn} and η_{syn} values that differ from all experimentally determined values, yielded a distribution of all likely C_{13} from which the maximum occurrence was selected based on the indicated, 'reasonable' bounds on C_{ij}* and *K_{meas}. (c) With defined C_{13} constants (different for the annealed and ashed dentine states), similar constraints and an assumed slight uncertainty in C_{13} were used to determine the maximum occurrence of C_{33}. (d) C_{11}, C_{12}, did not converge to unique solutions. Therefore, literature values were used to determine possible bounds on Young's moduli E_{11} and E_{33} and the basal/prism Poisson's ratios of dentine apatite crystals in the annealed and ashed states.*

2.5 Theoretical calculations of apatite stiffness tensors

Elastic constants of the entire stiffness tensor of c-Ap and ashed samples were computed by linear extrapolation based on previously reported MD simulation calculations [39]. Simulations for carbonated apatites containing 0, 1.5, 3.1, 6.3, 9.8, 13.4, 17.3, 24.1, 25.9, and 30 wt.% B-type carbonate substitution were extrapolated. The assumption in the model is that carbonate substitutes for phosphate. Simulations yielded estimated lattice spacing, surface energy, and elastic constants as well as the variability of the simulation as reported previously [39]. We have shown that the model was able to accurately replicate changes in atomic organization with decreasing carbonate levels in the c-Ap nanocrystals [39]. The reported simulations provide a range of possible elastic constant values for different carbonate concentrations, but they did not provide information at all the carbonate levels of interest for the different pig dentine states used. Therefore, using the distribution of the calculated C_{11}, C_{12}, C_{13}, and C_{33} at each composition from the reported MD model, elastic constants were linearly interpolated to match deformation of crystals comprising 0 to 30 wt.% carbonate. At each composition, 100 random values of resulting elastic constants were generated from a normal distribution of constants, with the mean

parameter defined by the average of the molecular dynamic simulation and the standard deviation determined from the variability of the model. This provided predictions for each carbonate level of interest. For this study on pig dentine, we focus on the properties of apatites with 0 wt.%

for ashed samples and 4 wt.% to 6 wt.% for the c-Ap.

2.6 STEM imaging

For measurements of crystal lengths [70], a pristine slice of pig root dentine, thinned by ion-milling to ~100 nm thickness, was investigated in a Philips CM12 TEM (Philips Electron Optics, Eindhoven, The Netherlands) operated at an acceleration voltage of 120 kV in both bright-field and dark-field imaging modes.

FIB-SEM milled conical nano pillar specimens of both pristine and ashed samples were imaged by an aberration-corrected high angle annular dark field (HAADF)-STEM, FEI Titan G2 (FEI Company, Hillsboro, Oregon, USA) at 200 kV, to observe the presence and morphology of the c-Ap particles.

2.7 3D APT elemental mapping

APT analysis of conical nano pillar specimens was performed in a CAMECA LEAP5000XS (Ametek, Berwyn, Pennsylvania, USA) using a 355 nm pulsed laser at rates of 100 kHz, 10 pJ/pulse, at 1.5% detection rates while maintaining the specimen temperature at 30 K. Measurements of ashed samples failed as these samples were too porous and brittle and hence unstable for APT chemical analysis.

2.8 Control experiments to determine mineral particle dimensions: X-ray versus TEM

Analysis of crystallite sizes (lengths, along the *c*-axis) by both X-ray and TEM were used to verify that no significant recrystallization took place in the c-Ap particles, due to our heat treatments, by comparison of the crystal lengths of annealed and ashed samples to previous measurements of pristine samples [49]. A Voigt analysis was used to determine the Gaussian and Lorentzian broadening contributions from which the averaged microstrain fluctuations, δ, and crystallite sizes, L, were determined [11]. To corroborate our X-ray results, measurements by dark-field TEM were used to directly visualize the lengths of several c-Ap crystals. Similar to what is observed by X-ray, TEM diffraction of the (002) reflections create arcs that are visible by electron microscopy, making it possible to collect dark-field images of coherently-scattering domains of crystals of apatite. It is thus possible to estimate the lengths of the crystals in the thinned sections, when they are appropriately oriented to scatter from the 0001 lattice planes (supplementary Fig. S3). In such images, the c-Ap crystals appear as bright lines (see [70], and as demonstrated also in figures 6 and 7 in [71]). The dark-field images were used to measure the lengths of a total of 48 individual crystals, whose dimensions were measured with Fiji [72].

2.9 Statistical analysis

The different types of data were analysed with different methods, adapted to the amount of data collected. The APT volume data for different elements (n > 30,000 datapoints) were analysed for correlation between Ca, P, N and C. Counts of all elements were plotted and linear regression revealed correlation coefficients and trends in the data. The elements P and C are of relevance for the work shown here.

Crystal size distributions measured manually in dark-field TEM images were analysed by descriptive statistics (Excel, Microsoft Office 365), and tested for normality using the Shapiro-Wilk test (SciPy toolbox).

The X-ray diffraction peak fits were analysed for normality using the Shapiro-Wilk test. Results of broadening analysis yielding crystallite sizes and microstrain fluctuations are presented as means and standard deviations. Probability distributions of the synthetic K_{syn} and η_{syn} were generated to fall within 5% of K_{meas} and η_{meas}, as determined from gradients in *a*- and *c*- lattice parameters of different samples. The large number of synthetically generated K_{syn} and η_{syn} resulted in large normally distributed datasets the maxima of which were used to define elastic properties based on the different models described. The groups of different moduli obtained for each heat treatment and each model, are precise up to the 4 GPa bin size used and therefore uncertainties in each model (in C_{13} and C_{33}) were compared by a t-test with significance set at $p < 0.05$.

3. Results

3.1 Structural observations

The composite structure and main elements comprising intertubular pig dentine were studied by combining HAADF-STEM and APT. The small diameter conical nano pillars of dentine observed from 2 different angles (rotated by 30° in the STEM, Fig. 4) reveal parallel, elongated, dense platelets (red arrows) in both the pristine and ashed dentine states. These mainly differ in the organic content, which is completely missing in the latter. As can be seen in the micrograph, either isolated or clusters of elongated objects appear as stripes, completely dominating the tissue, with regions of low density seen to occupy spaces between them. These objects, corresponding to the c-Ap crystals, are plates, and in the pristine state, they are in contact with electron-transparent organic material. Between crystals, we assume that water may freely pass through open structural porosity, when applying force isotropically with increasing hydrostatic pressure. Rotation of the nano pillars along the long sample axis (e.g. 30° to the left, Figs. 4b, 4d) exemplifies how the striped appearance of some of the crystals vanishes while the dense objects attain appreciable widths, typical of rotation of plate-shaped structures. In many regions there appear to be clusters rather than isolated crystals. These observations are well reproduced in a 3D reconstruction of STEM tomography of the ashed dentine (supplementary Video S4). In such an ashed sample, protein fibrils are burned out by oxidation, yet these samples never disintegrate into separated mineral needles which matches previous reports for bone, treated to remove collagen by wet oxidation [5, 73, 74].

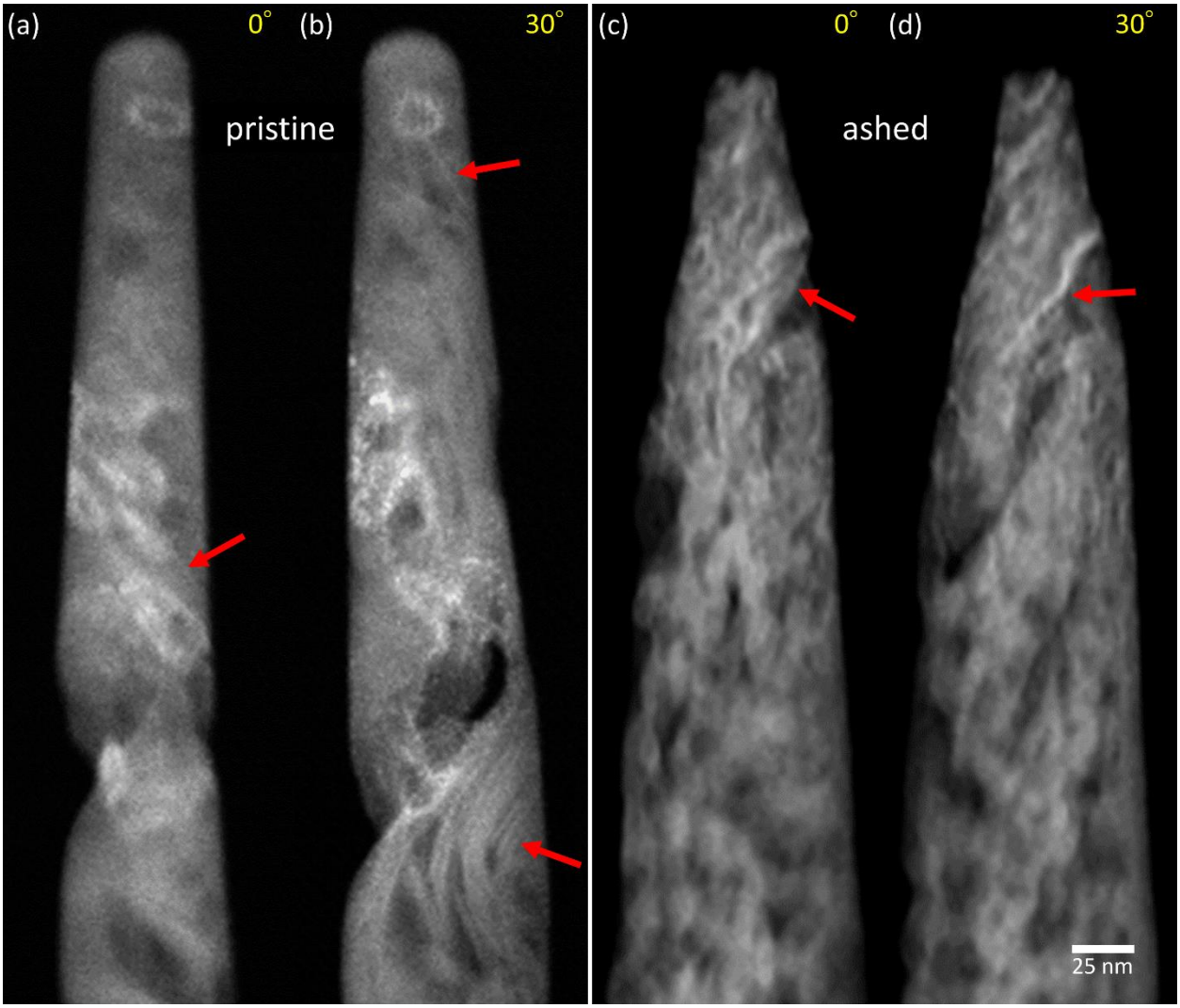

Fig. 4: HAADF-STEM images of pristine and ashed pig dentine confirm the presence of nano plates. *(a) Dense elongated striped objects (red arrows) dominate the structure of pristine tissue, as observed in conical nano pillars of intertubular dentine prepared for APT analysis. In some regions it is easy to observe clearly demarcated lines, corresponding to the thinner aspect of high density platelets. (b) Upon rotation, e.g. by 30°, the striped objects in pristine dentine become blurred and wider, ruling out the presence of significant amounts of needles. (c) Ashed pig dentine samples (550 °C for 10 hours) exhibit high porosity due to burn-out of the organic phase but still reveal the same platy morphology when rotated similarly to pristine samples, as shown in (d). Ashing does not seem to lead to appreciable recrystallization or crystal growth. Bright contrast indicates higher density.*

Compositional information and spatial relations between mineral and protein were examined by APT collected from pristine dentine, obtained from central regions of several conical nano pillars. Typical 3D surface renderings reveal protein rich domains dominated by nitrogen (N) in close contact with mineralized domains rich in calcium (Ca), as seen in Fig. 5a. The same complementary image is observed for carbon (C) and phosphorus (P). Cross-sectional slices in this data (Fig. 5b, corresponding to the slices marked blue in Fig. 5a) yield 2D composition maps, showing domains rich in mineral, comprising mainly

Ca (red arrows, Fig. 5b) and P. These are the platy c-Ap crystals of dentine. Most of the Ca (and P) signal arises from the regions that are distinct from adjacent protein rich domains, as seen by the distributions of the element N. Note especially how regions rich in protein are poor in Ca and vice-versa. The element C dominates the protein domains but is also found in appreciable amounts in the mineralized regions of the crystals. This provides additional proof that in the pristine samples, C is present in the Ca-rich domains and is not limited to the collagen protein backbone. Using Ca and N as masks in the 3D data, regions of high mineral (Ca > 34%) and regions of high protein (N > 5.2%) were selected. Comparison of the normalized concentrations of C and P yielded an inverse linear correlation (r = -0.84) for the crystal domains. No such high correlation can be seen in the protein rich regions of the imaged volume.

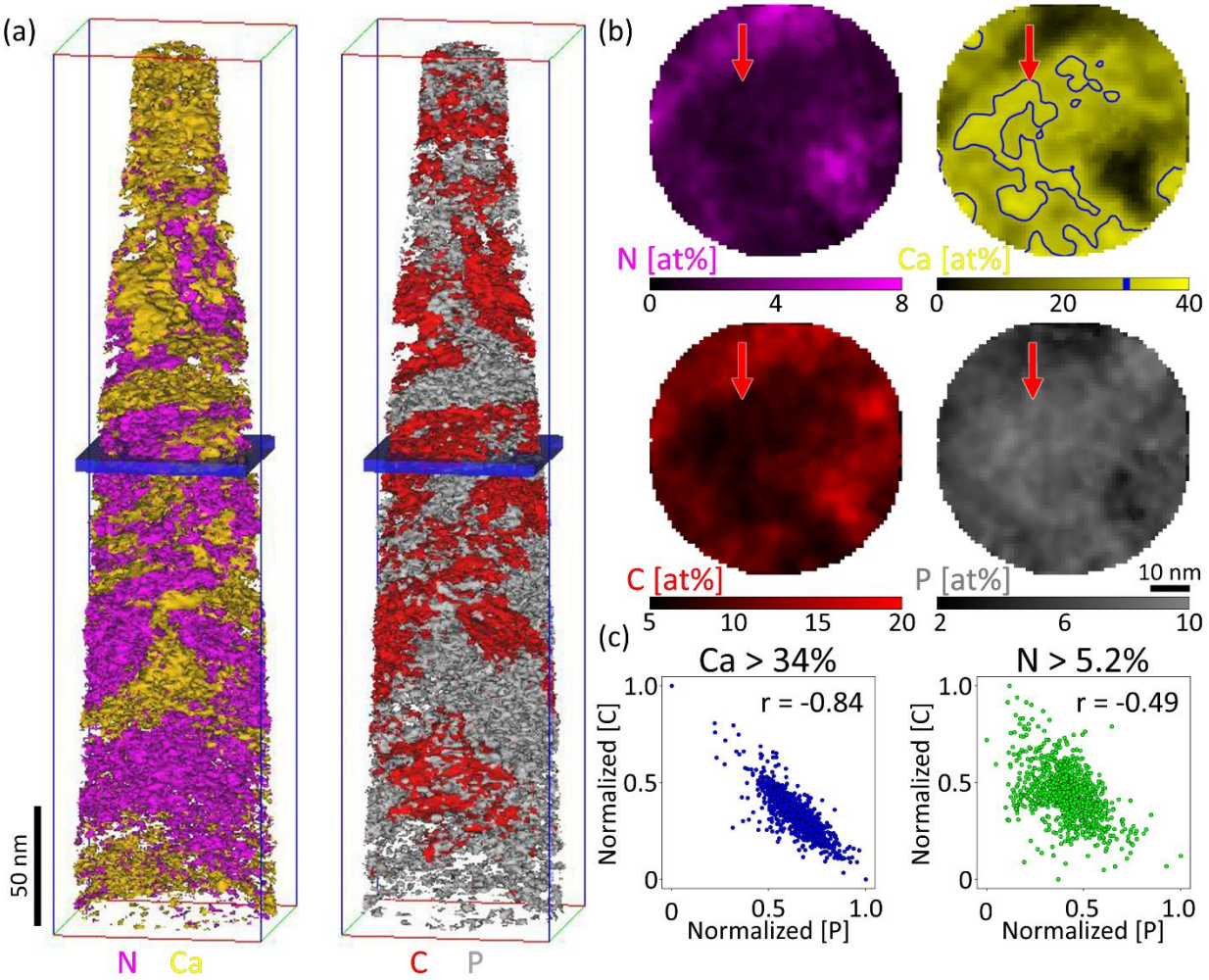

Fig. 5: 3D renderings of the atomic composition of pristine pig dentine. *(a) Typical 3D maps obtained by APT. Iso-concentration-surfaces depict the distributions of Ca, N, C and P. The following threshold values were chosen for these rendering: 29.0 at.% for Ca, 3.0 at.% for N, 13.0 at.% for C and 8.0 at.% for P. (b) Slices in the 3D data reveal the spatial distribution of the main mineral and organic components of*

mineralized collagen fibres in the APT data, as indicated by the blue region in the renderings in (a). The maps allow direct comparisons of the distributions of N, Ca, C and P. The N map well depicts domains of protein, showing that this element is rather confined to regions between the Ca rich domains. While it is not possible to directly visualize carbonate (CO_3^{2-}), regions with high concentrations of Ca and P may be assumed to comprise mainly crystalline c-Ap. (c) Correlation between normalized at.% concentration of [C] as a function of [P] in the APT volume of ~500 x 60 x 60 nm^3 in high mineral (Ca > 34%) versus high protein (N > 5.2%) zones corresponding to crystalline and collagen domains of a mineralized collagen fibre. Analysis of n = 980 different points reveals an inverse relationship between P and C in the mineral rich domains (r = -0.84), consistent with B-type substitution where carbonate replaces phosphate sites in the crystal. No such correlation is observed in the protein rich domains.

Bright-field TEM images (Fig. 6) show the recurring arrangement of platelets in the tissue aligned along the general axis of the low density polymer fibrils. Note that the contrasts presented by HAADF-STEM and bright-field TEM are inverted. Both longitudinal and cross-sectional TEM views reveal mineral plates suspended within a low density (protein fibril) matrix. Both top and side edge-on views (Fig. 6a and 6b, note dense silhouettes of short lines marked by red arrows) confirm the omnipresence of plates in pig root dentine. Selected area diffraction (SAED, supplementary Fig. S3) confirms that along the orientation of the fibres, the *c*-axis (and the corresponding arcs corresponding to the 002 reflections) matches the elongated crystal axis (seen running vertically in Fig. 6a). Dark-field (DF) TEM imaging (supplementary Fig. S3) of the ion milled samples produced estimations of the crystal dimensions. For n = 48 crystals we find an average length L_{TEM} = 20.6 ± 8.7 nm (standard deviation). The distribution of crystal sizes is however asymmetric with a statistical skewness of +0.93 suggesting that the mean crystal size is somewhat larger than what is visible by DF-TEM.

Voigt fitting (see [11] and [69] for details) of X-ray measurements of unloaded samples revealed average *c*-axis crystal lengths of 34.2 ± 3.8 nm and 34.5 ± 2.1 nm for annealed and ashed dentine samples, respectively (supplementary Fig. S5). These sizes are not statistically significantly different. Microstrain fluctuations of up to 0.339 ± 0.049% in the annealed samples, increasing substantially to 0.443 ± 0.012% in the ashed samples (t-test, $P < 0.05$).

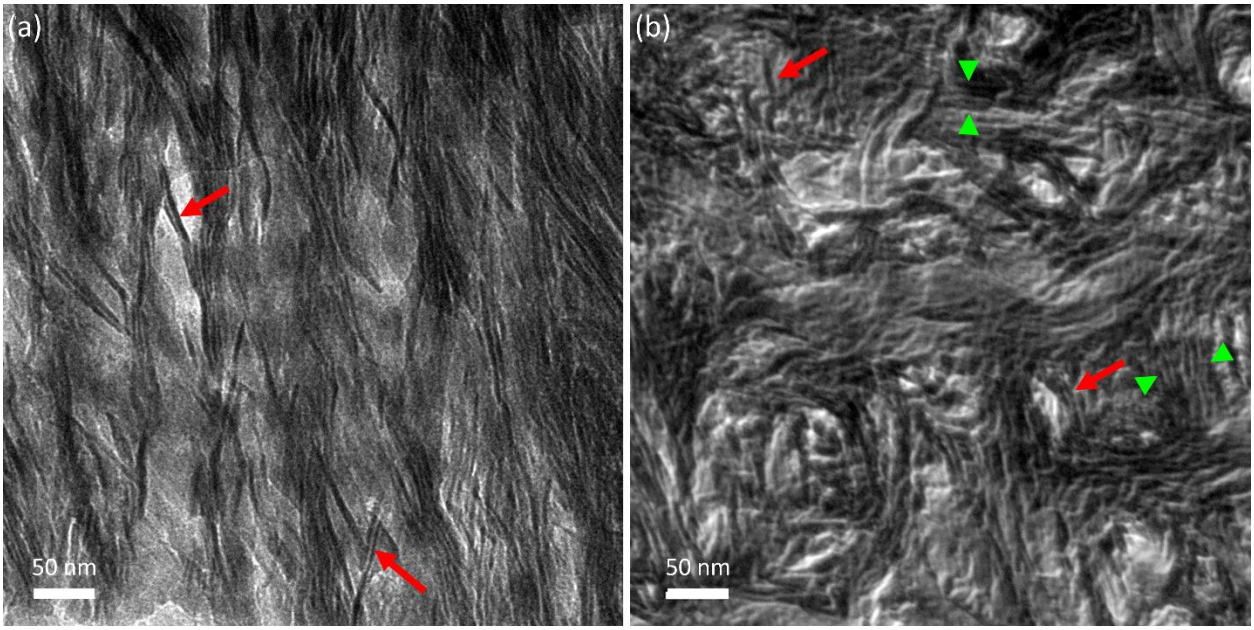

Fig. 6: TEM images of ion-milled thinned sections of pig dentine. *(a) Crystals observed from a side profile appear as dark elongated objects of high density in bright-field (BF) TEM. Note inverse contrast as compared to the HAADF-STEM longitudinal section (Fig. 4a). BF-TEM reveals bundles of parallel-oriented collagen fibril silhouettes about 50 nm in width, comprising stacks of mineral crystals. Red arrows point to dense objects viewed edge on, matching observations of polycrystalline apatite plates in bone [5]. The c-axis is oriented approximately vertically in this micrograph, compare supplementary figure S3 and the associated diffraction pattern therein. (b) Cross-section view: many single plates are viewed out of plane, on edge (red arrows), corresponding to an orientation that is orthogonal to that shown in panel a, as seen along the collagen and c-axis of the crystals. The crystals are thus mostly plate shaped, and they bunch into packed clusters (e.g. between the green arrowheads). Single "stacks of cards" [79] or "mineral lamellae" [71] prevail in the tissue. Along this view, at the edges of straight segments of crystals, other crystals often appear to fuse together at angles. Thus, the dense clusters of crystals appear to "wrap" around low density (brighter) sites of protein viewed on edge, similar to bone [5, 73].*

3.2 Deformation analysis

All series of X-ray diffraction measurements under increasing hydrostatic pressure revealed reversible linear decreases in both *a*- and *c*-lattice parameters of the crystals. The mean and standard deviations for the lattice parameters were a = 9.4495 ± 0.0123 Å, c = 6.8799 ± 0.0066 Å for annealed and a = 9.4405 ± 0.0144 Å, c = 6.8774 ± 0.0042 Å for ashed samples. We note however, that lattice parameters vary substantially across the root thickness as previously demonstrated [11] and as is evident from the standard deviations of the samples. For further analysis we focus on the relative change in d-spacings of each sample, with respect to its own uncompressed lattice parameters. The *a*- and *c*-lattice parameter strains were obtained by normalization at each pressurized state with respect to the initial hydrated reference state at a hydrostatic pressure of 5 MPa. All samples exhibit reversible deformation of the apatite nanoparticles. The trends in both annealed and ashed apatite crystal deformation are shown as normalized lattice parameter strains in supplementary Fig. S1. The changes of *a*-/*c*-lattice parameters

were used to calculate both bulk moduli (K) and lattice strain ratios (η) of each sample. The resulting mean measured values and standard deviations are plotted in figure 7, amounting to 85.1 ± 9.6 and 85.2 ± 2.5 GPa for the annealed and ashed dentine samples, respectively. The lattice strain ratios (η) were 1.93 ± 0.5 and 1.35 ± 0.18 for the annealed and ashed samples, respectively

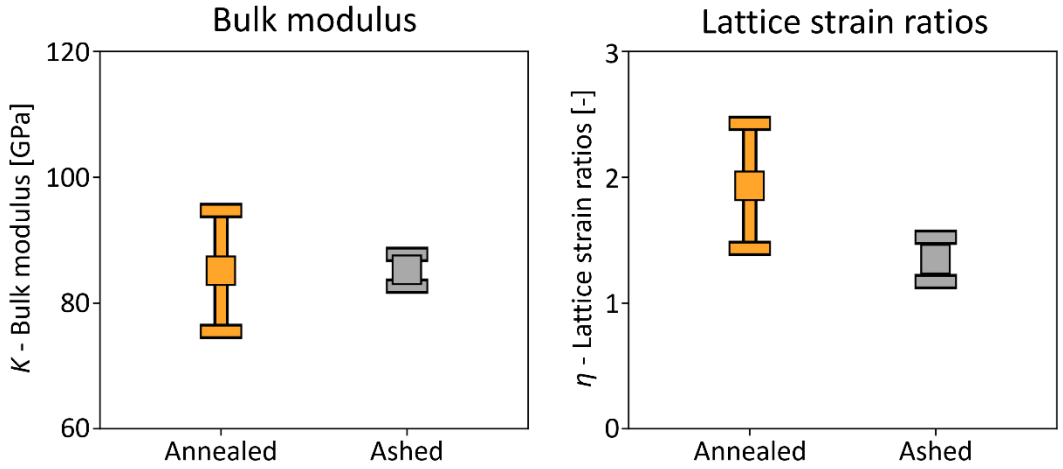

Fig. 7: Experimentally measured bulk moduli (K) and lattice strain ratios (η) in annealed c-Ap versus decarbonated nanocrystals of pig dentine. *Plots show means and standard deviations. Note the large variation in the annealed samples.*

Based on the fitting procedure described in section 2.4, and following all comparisons with the experimentally derived K_{meas} and η_{meas} elastic constant pairs C_{13} and C_{33} were calculated for the annealed (visibly brown and carbon rich) and ashed (decarbonated) dentine samples. These results, alongside with recalculations of previously measured samples that were not heat treated (pristine samples), published in [49], are presented in supplementary table S6. By taking C_{11} and C_{12} from simulations reported in the literature, it is possible to calculate Young's moduli and Poisson's ratios for both c-Ap and the decarbonated apatite nanocrystals. Results based on Tofail *et al.* [22], Menéndez-Proupin *et al.* [40], and Deymier *et al.* [39] are shown in table 1 and the means and standard deviations of the results are presented visually in figure 8. Thus, annealed c-Ap samples have elastic moduli of $E_{11} \approx 102 \pm 7$ GPa and $E_{33} \approx 109 \pm 8$ GPa whereas ashed samples show $E_{11} \approx 107 \pm 7$ GPa and $E_{33} \approx 128 \pm 6$ GPa. Recalculations applied to previous measurements of pristine samples, and employing the same procedures as described in 2.3 and 2.4, serve for comparison. These recalculations yielded $E_{11} \approx 104 \pm 7$ GPa and $E_{33} \approx 115 \pm 7$ GPa for pristine dentine, corresponding to the present results for the annealed c-Ap crystals. As summarized in table 1, regardless of the model used, E_{33} shows an increase of ~17% in stiffness upon c-Ap crystal ashing. In all models, t-test comparison between annealed and ashed samples revealed a significant increase in modulus upon ashing.

Poisson's ratios for the different samples were calculated according to eqs. 5-7. The values of Poisson's ratios in the basal hexagonal plane are higher than the values in the prismatic planes of the apatite crystals. These results are shown in the lower panel of table 1. The average prism and basal Poisson's ratios (varying slightly in the different models) for annealed dentine are 0.25 ± 0.02 and 0.36 ± 0.04. Curiously, although there is a difference of >50% between the basal and prismatic orientations in all models, when taken on average, they almost match the idealised 0.3 values commonly assumed in the

literature. There was a minimal effect of the different C_{11} and C_{12} models, as seen in table 1. The ashed samples have slightly lower Poisson's ratios, averaging 0.24 ± 0.02 and 0.32 ± 0.04, corresponding to v_{basal} and v_{prism} respectively.

Table 1: Young's moduli and Poisson's ratios of annealed, ashed, and pristine dentine.

	This work				Previous data	
	Annealed [GPa]		Ashed [GPa]		Pristine* [GPa]	
Calculated Young's modulus with C_{11} and C_{12} estimates from	E_{11}	E_{33}	E_{11}	E_{33}	E_{11}	E_{33}
Tofail *et al.* [22]	104.9 ± 1.5	113.4 ± 5.4	108.7 ± 1.1	131.2 ± 4.9	106.7 ± 1.3	118.5 ± 5.2
Menéndez-Proupin *et al.* [44]	92.5 ± 2.4	102.3 ± 6.3	98.2 ± 1.7	122.7 ± 5.8	95.2 ± 2.1	108.7 ± 6.1
Deymier *et al.* [39]	109 ± 1.9	111.2 ± 5.6	113.7 ± 1.4	129.5 ± 5.1	111.2 ± 1.7	116.5 ± 5.3
Calculated Poisson's ratio with C_{11} and C_{12} estimates from	v_{prism}	v_{basal}	v_{prism}	v_{basal}	v_{prism}	v_{basal}
Tofail *et al.* [22]	0.28 ± 0	0.33 ± 0.02	0.26 ± 0	0.28 ± 0.02	0.27 ± 0	0.31 ± 0.02
Menéndez-Proupin *et al.* [44]	0.22 ± 0	0.42 ± 0.02	0.21 ± 0	0.36 ± 0.02	0.22 ± 0	0.39 ± 0.02
Deymier *et al.* [39]	0.25 ± 0	0.34 ± 0.02	0.24 ± 0	0.3 ± 0.02	0.25 ± 0	0.32 ± 0.02

*re-calculated based from measurement of Forien *et al.* [49]

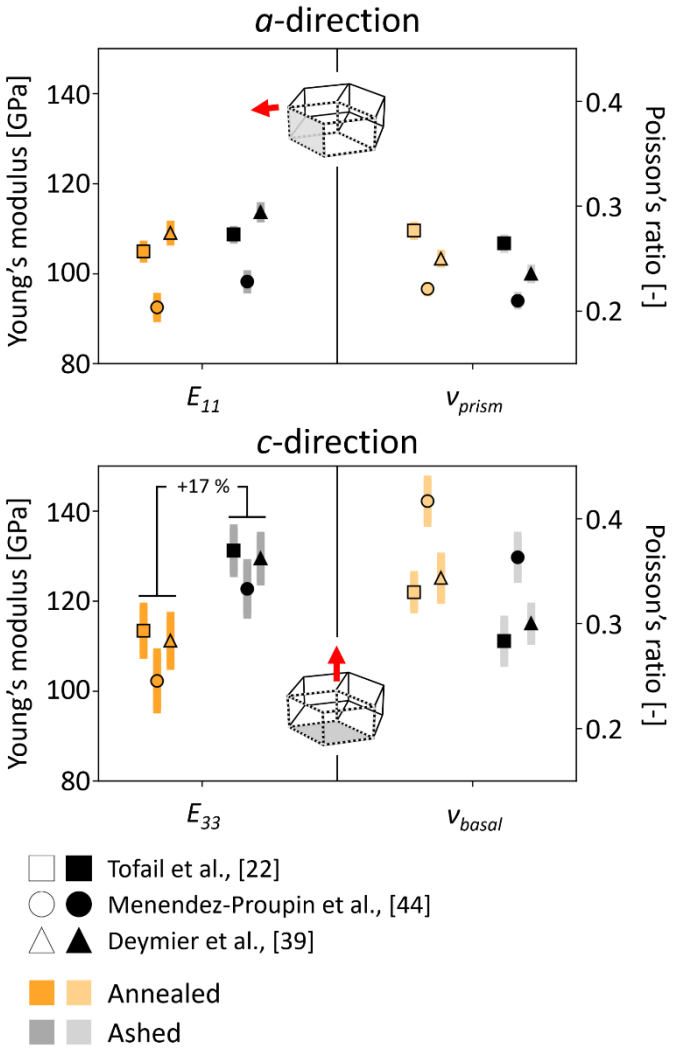

Fig. 8: Young's moduli (E_{11}, E_{33}) and Poisson's ratios (v_{prism}, v_{basal}) of annealed and decarbonated crystals of apatite along the a- and c-lattice directions. *Ashed samples are marked with filled-in symbols. For each model, the maximum occurrence of C_{33} and C_{13} were combined with literature reported models of C_{11} and C_{12} [22,39,40] to estimate the modulus and Poisson's ratios using equations 5-6-7. Uncertainty due to the 4 GPa bin size of C_{13} and C_{33} is the standard deviation, as indicated by the vertical lines.*

3.3 Extrapolation from MD numerical simulations

The experimental bulk moduli and lattice strain ratio results were used as input for mechanical constant estimation based on previously reported MD simulations that account for variations in carbonate content [39]. The simulated predicted Young's moduli and Poisson's ratios as a function of increasing carbonate content are presented in table 2. These simulations consistently revealed an increased softening effect of higher CO_3^{2-} inclusion into the c-Ap crystals. Whereas an addition of 4% carbonate leads to a reduction of ~3% in E_{11} and a reduction of 9% in E_{33}, the inclusion of 6% CO_3^{2-} in the nanocrystals predicted a 12% reduction in E_{11} and 21% in E_{33}. Note however that the MD simulated stiffness values are

generally ~10 to ~15% higher and the Poisson's ratio values 10 ~20% lower than the results that we obtained experimentally.

Table 2: Predicted results of Young's moduli and Poisson's ratios for c-Ap nanocrystals containing 0, 4 and 6 wt.% carbonate, based on molecular dynamic simulation probabilities.

	Carbonate wt.%					
	0%		4%		6%	
Simulated Young's modulus [GPa]	E_{11}	E_{33}	E_{11}	E_{33}	E_{11}	E_{33}
	119	151	115	138	104	119

Simulated Poisson's ratio [-]	N_{prism}	N_{basal}	v_{prism}	v_{basal}	v_{prism}	v_{basal}
	0.28	0.26	0.32	0.24	0.29	0.32

4. Discussion

It is challenging to mechanically load and reproducibly measure deformation in biogenic c-Ap nanoparticles. In this work, a combination of *in situ* hydrostatic pressurization and diffraction analysis combined with TEM/STEM imaging and APT made it possible to determine properties of the apatite nanocrystals, while ascertaining the nanostructural arrangement of the natural and ashed tissue. We make use of computational resampling of data obtained experimentally (XRD) and data from simulations (molecular dynamics, MD). Our data yield the fundamental elastic properties (Young's moduli and Poisson's ratio) for both carbonated and decarbonated biogenic apatite in tooth dentine.

4.1 Mechanical response to load

Our results show that biogenic c-Ap crystals in mineralized collagen fibrils of dentine are substantially softer than ashed, decarbonated crystals. Hydrostatic pressurization up to 400 MPa, employing high energy diffraction measurements, provided non-contact, *in situ*, quantitative estimations of deformation in crystals within the dentine biocomposite. We find that the c-Ap crystals deform appreciably almost 20% more along the *c*-axis, as compared with biogenic apatite crystals that were decarbonated for 10 hours at a temperature of 550 °C. The deformation analysis revealed a range of K_{meas} (Fig. 7) between the different samples, indicative of inter-sample variability, which is typical for specimens of biological origin. Our results quantify deformations in the *a*- and *c*-lattice parameters, thus the variations in the observed compressibility are due to components of biogenic apatite, most likely, the carbonate content within the crystal lattice itself [82]. A clear advantage of performing X-ray experiments at high energy is that the measurements are non-destructive to the crystals. By testing samples in which the organic component was destroyed, we exclude radiation damage effects. Both TEM and STEM

demonstrate the presence of narrow spaces between the elongated surfaces of adjacent mineral crystals. Such spaces likely accommodate water in dentine, reportedly comprising ~20 vol.% in the pristine state. Already half a century back, Lim and Liboff [56], proposed that water may be tightly bound to and can be shared between both the mineral and organics. The presence of the above mentioned spaces is fully consistent with this possibility. Our microscopy images support the assumption that these spaces are linked, creating open porosity largely accessible to water, which upon pressurization is able to deform the crystals, as demonstrated by XRD. Although water cannot directly be visualized by our methods, its capacity to induce deformation of crystals in the dentine nanocomposite was recently proven [11]. Specifically, we previously showed how dehydration leads to significant compression along the c-Ap crystals due to expelling of water and shrinkage of the collagen fibrils. Therefore, it was ideal to use water as a means for applying pressure to crystals embedded within the dentine slabs. Indeed, with this method we could reliably induce sub-nanometre deformations directly to the c-Ap crystals resulting in reversible changes in the lattice d-spacings. By heat treatment, we destroy the collagen either by annealing at 250 °C or by extensive ashing. We thus believe that deformation of the nanocrystals in this work was essentially due to the hydrostatic pressure that we apply. Heat treatments however extensively dry the samples, making rehydration necessary prior to hydrostatic loading. Water was therefore initially used to apply mild hydrostatic pressure allowing equilibration prior to diffraction measurements. For the ashed samples, we are certain that rehydration was rather complete, because following an initial *a*-/*c*-lattice relaxation in the first 10 minutes of wetting, XRD revealed no further peak shifts, which we use as an indication that these samples reached full hydration. The annealed samples are more difficult to hydrate under the limited time available for *in situ* measurements. Nevertheless, air trapped in the system also becomes compressed such that deformation of the nanocrystals is expected, and was demonstrated, in all cases. Indeed, following hydrostatic compression, diffraction revealed elastic deformation of the nanocrystals, which was fully recoverable upon pressure release.

4.2 Microstructural observations

In conjunction with supporting observations by TEM, STEM and APT, we clearly identified apatite plate-shaped crystals about 5 nm thick and ~35 nm long, often arranged into aggregates, yet always seen as separable discrete objects. The main inorganic morphologies observed in mineralized collagen fibres of dentine are thus plates, as seen by longitudinal and cross-sectional views (Fig. 6). Our images match many reports of bony tissue nanostructures in recent decades [2,3,71,75], somewhat contrary to resurging suggestions that needles are the structural motifs in these biogenic nanocomposites [76,80]. The STEM tomography of ashed FIB milled conical nano pillars (S4 supplementary video) again demonstrates the plate-shaped morphologies. Due to electron radiation damage, we were not able to obtain such tomographic images of pristine samples, because disintegration and motion are caused by interactions of the electrons with the protein, leading to release of residual stresses entrapped in the dry native tissue [12]. TEM shows that multiple crystals are often seen to be stacked (Fig. 6b green arrowheads and in the supplementary video S4), separated by thin gaps, and forming larger clusters (sometimes termed “mineral lamellae” [5,71,73,75]). Multiple crystals appear to fuse at the edges, often oriented at angles, creating curved, arc-like architectures (green arrowheads). The observed nanogeometry of plates in dentine is probably essential for efficient load transfer across the large surfaces of the mineral particles, in contact with other plates or with the organic network of collagen fibrils. Dentine, similar to ivory and other bony

nanocomposites, exhibits the usual orientation, morphology and composition of mineralized collagen fibres. In these fibres, clusters of plate-shaped crystals have been described as “stacked cards” [79] comprising crystal plates, within a low density (polymer) matrix.

By virtue of the length-scales involved, both HAADF-STEM and APT results are extremely local, typically spanning lateral dimensions of less than 300 nm. They are therefore better understood when placed in context of larger segments of the tissue, e.g. by examining lower resolution bright-field TEM. Such images however yield a mean low crystal length (~21 nm) with a rather positively skewed distribution, based on the limited number (n = 48) of crystals that can be measured manually. This distribution suggests that there is an over representation of smaller crystals in the ion milled sections. There are two possible reasons that may explain why sizes by TEM are ~30% smaller than crystal length estimates (so called “coherent scattering length”) by X-ray broadening analysis. On the one hand, TEM samples undergo thin (~100 nm) sectioning, that may lead to preferential removal of the larger crystals, leaving the smaller crystals in the field of view. On the other hand there may be substantial deformation of the crystals in the vacuum-dry dentine samples, leading to partial bending that excludes Bragg’s condition needed to attain the DF contrast [11]. Both causes, as well as uncertainty in detection of crystal dimension, lead to selective elimination of larger crystals in the DF images. The mean crystal lengths in the dentine bulk are thus highly likely to be somewhat greater than ~21 nm, suggesting that the ~35 nm results obtained by X-ray broadening analysis of the 002 reflection is more representative of the average nanocrystal lengths in dentine. Whatever the case may be, direct XRD broadening comparison between annealed and ashed samples and observations of similar dimensions as compared with pristine samples show that neither annealing at 250 °C for 1 hour nor ashing at 550 °C for 10 hours lead to appreciable recrystallization. This matches previous reports showing grain growth in samples treated at temperatures that are far higher than our ashing temperature of 550 °C [59,77,78]. The combined TEM and X-ray analyses suggest therefore that heat treatment in our experiment had negligible effects on the platy morphologies of the apatite nanocrystals of dentine.

4.3 Effects of removal of carbonate by heat treatment

When heated in air to high temperatures (>600 ^{o}C), biogenic c-Ap undergoes various chemical changes and recrystallization [77]. Lower temperatures are however sufficient to oxidize the organic matter through reaction with atmospheric O_2. Several reports have quantified the decrease in the CO_3^{2-} content in c-Ap nanocrystals of dentine and bone, treated at temperatures that are lower than 600 ^{o}C. Using the relation proposed by Ou-Yang *et al.* [83] we converted FTIR peak ratios reported by Greiner *et al.* [59] to CO_3^{-2} wt.% estimates (supplementary Fig. S7). Data from Greiner *et al.* demonstrates a gradual steady loss of carbonate from bone during heating, with native CO_3^{2-} decreasing from 2 wt.%, which is similar to values reported for pig dentine [51]. Removal of CO_3^{2-} by heating has been associated with the appearance of OH^- in heat-treated c-Ap crystals [81]. Although the chemistry of the process is not well described, it probably involves the reaction of acid phosphate (HPO_4^{2-}), which is a component of all biological c-Ap [84]. In heat treated c-Ap, HPO_4^{2-} and CO_3^{2-} most likely react, according to:

$$CO_3^{2-} + HPO_4^{2-} \rightarrow CO_2 + PO_4^{3-} + OH^- \quad (8)$$

The emergence of OH^- is best demonstrated by vibrational spectroscopy that routinely reveals its presence upon heating [81], accompanied by loss of HPO_4^{2-}. In heat-treated apatite, IR spectroscopy detects hydroxyl groups at temperatures exceeding 400 ^oC [59]. We thus believe that the reaction of eq. (8) takes place also in our samples. Note however, that we kept the temperature of ashing sufficiently low (550 ^oC) so as to prevent recrystallization or growth of the mineral particles [59,61,77]. Our chosen temperature of ashing was thus sufficiently high so as to completely burn out all the organics while removing as much of the carbonate from within the c-Ap as possible. Indeed, our line broadening Voigt analysis showed no significant difference in the mean crystallite lengths before and after exposure to 550 °C for 10 hours (Fig. S5). Since ashing in our experiment lasted longer than previous reports [51,56,59], we expect that less than 0.5 wt.% CO_3^{2-} remains in the decarbonated crystals, assuming that ~80% of CO_3^{2-} is removed, as previously suggested [56,85]. Our ashed samples thus contain significantly reduced levels of carbonate, as compared with the native pig tooth biogenic c-Ap. These crystals reveal an impressive increase in the E_{33} Young's moduli, amounting to 17% along the *c*-axis. We thus demonstrate experimentally that removal of carbonate stiffens the apatite nanocrystals significantly, but primarily along the elongated plate axis. These results well match previous MD simulation predictions [39], as applied to our samples and as shown in table 2.

Our APT results directly demonstrated that in native pig dentine, appreciable amounts of carbon (C) exist within the mineralized Ca rich domains of the nanocomposite. In such domains, which presumably correspond to crystalline regions in the mineralized collagen fibres, we observe an inverse, rather high correlation between C and P (r = -0.84). APT does not allow us to decouple oxygen in CO_3^{2-} from other locations where O is found in the crystal lattice, e.g. HPO_4^{2-}. However, the presence of several at.% of C is consistent with numerous reports of appreciable amounts of carbonate residing in the c-Ap crystals of dentine (summarized in [19,84]). CO_3^{2-} is therefore not confined to the outer crystal boundaries of c-Ap particles. In the Ca rich domains, C is uniformly distributed throughout - and forms a part of - the mineral crystal lattice of pristine biogenic apatite of tooth dentine, where, in the form of CO_3^{2-}, it distorts the crystal lattice parameters [19]. It was not possible for us to obtain APT measurements of conical nano pillars of ashed dentine (see supporting information video S4), due to disintegration of the brittle and highly porous samples.

The APT results help explain the ~30% increase in X-ray determined microstrain fluctuations upon ashing, a recurring observation of ours, as previously reported [11]. We propose that with removal of carbonate, local atomic disorder increases within the affected apatite nanocrystals. It is likely that CO_2 is not uniformly removed from the c-Ap crystals during ashing. We hypothesize that a minimal, non-uniform distribution of carbonate remains in the crystal lattice, causing a substantial increase in microstrain fluctuations in the ashed samples. Indeed it is possible that preferentially, e.g. at sites near the surfaces, ashing mobilizes CO_3^{2-} (eq. 8) to be readily substituted by thermodynamically more stable PO_4^{3-} groups. This observation is different from what is seen in the annealed samples, where exposure to heating at 250 °C mainly destroys the protein [56], resulting in release of much of the residual stress known to exist in dehydrated dentine [12]. Overall, removal of carbonate, which results in ~5% denser unit cells [84] leads to stiffer crystals, where especially along the *c*-axis, the modulus E_{33} increases. Direct comparison of deformation in the annealed samples with previous measurements on pristine dentine [49] and recalculation of moduli (E_{11}, E_{33}) as described in sections 2.3 and 2.4 (Table 1) show negligible differences between pristine (previously reported) and annealed samples (measured here). Interestingly, results of

MD simulations (Table 2) based on our measurements, predict even higher stiffening of E_{33} for crystals that are completely devoid of CO_3^{2-}. However, we were not able to validate this experimentally. We conclude therefore that removal of ~80% carbonate from biogenic c-Ap crystals results in crystals that are ~17% stiffer, along the *c*-axis as compared with natural biogenic c-Ap crystals.

We observe linearly increasing compressive strain during pressurization, resulting in deformation that is similar to values reported previously for hydrated pristine dentine [49]. Our bulk moduli K are within the range reported for geological apatite and for computer simulations of hydroxyapatite compression [26,29,41], as surveyed in Table 1 of Forien *et al.* [49]. Whereas for the annealed samples, the deformation along the *a*-axis is almost twice as high as the deformation along the *c*-axis, in the ashed samples this changes, with η decreasing such that the ratio of deformations becomes more similar along both axes. Note the small spread observed for both K and η in the ashed samples from different teeth: we hypothesize that this is related to the removal of CO_3^{-2} from within the c-Ap crystals leading to a smaller variability between ashed samples, where composition becomes less biologically variable.

Our mechanical stiffness values obtained for both carbonated and de-carbonated HAp crystals of dentine are based on matching experimental compression measurements with synthetically derived elastic constants. To obtain distributions of these constants, initially all possible combinations of C_{11}, C_{12}. C_{13} and C_{33} were generated in the range of 0-200 GPa and all were used to test for possible matches with the deformation response of the hexagonal crystals of hydroxyapatite. The large (6,250,000) number of combinations defined distributions of constants that made it possible to identify K_{syn} and η_{syn} that are very close to the ones measured for our samples (K_{meas} and η_{meas}). The constants were therefore identified in a stepwise manner (Fig. 3): a narrow peak in the distribution of C_{13} values emerged, based on matching the experimental data with simulations using restricted K, C_{13} and C_{33} ranges. In a second step, restriction of C_{13} to a small range (±2 GPa) around the value found in the first step yielded a confined, well defined distribution of C_{33} values corresponding to experiments. Our approach therefore provides experimentally-backed average estimates of only two of the four elastic constants of the c-Ap crystals. Consequently, calculation of the elastic moduli E_{11} and E_{33} and respective Poisson's ratios requires making use of simulation and other estimated results available in the literature. Nevertheless, and regardless of the models used, all results clearly demonstrate a substantial stiffening effect of removal of the CO_3^{2-} from c-Ap in the dentine nanocrystals. It may be speculated, that in addition to the well-known strategy of stiffening by increasing mineral content, nature could utilize an additional level of control in biogenic c-Ap nanocomposites by strategically varying carbonate content, to stiffen or soften the nanoparticles of mineralized collagen fibrils depending on location within the tooth. Further work is needed to explore this.

5. Conclusions

The present study quantifies the elastic moduli of c-Ap nanocrystals, finding that following ashing the nanocrystals become significantly stiffer. We report the effects of heat treatments on the mechanical properties of biogenic c-Ap particles of pig tooth dentine. X-ray diffraction measurements performed on mm-thick samples under increasing hydrostatic compression revealed deformation along the *a*- and *c*-lattice axes of annealed and ashed dentine. Bulk modulus (K_{meas}) and lattice strain ratios (η_{meas}) determined from the peak shifts of the Debye rings fall within the range of values reported for geological hydroxyapatites. Following comparison of sample measurements with all possible combinations of

synthetically-generated stiffness constants we identify realistic distributions of K_{syn} and η_{syn}. Coupled with TEM and APT, our work allows us to conclude:

a. It was possible to experimentally determine, for annealed and ashed dentine samples, two of the c-Ap hexagonal crystal symmetry elastic constants: C_{13} = 62 and 54 GPa and C_{33} = 154 and 162 GPa for carbonated and de-carbonated biogenic apatite nanocrystals, respectively.
b. Calculations yielded refined estimates of two Young's moduli of carbonated and decarbonated biogenic apatite (Table 1). On average, there was a 5% increase in stiffness orthogonal to the crystal long axis (increasing from 102 ± 7 GPa to 107 ± 7 GPa) and a 17% increase in stiffness of E_{33} along the crystals (increasing from 109 ± 8 GPa to 128 ± 6 GPa) for annealed and ashed samples, respectively. Removal of carbonate increases the stiffness 3 times as much along the *c*-axis, as compared with the *a*-axis of c-Ap.
c. Poisson's ratios (0.25 ± 0.02 and 0.36 ± 0.04 for the prism and basal plane of annealed dentine and 0.24 ± 0.02 and 0.32 ± 0.04 for ashed dentine) show statistically significant but small differences between carbonated and decarbonated biogenic apatite crystals. A difference of ~44% higher basal Poisson's ratio of c-Ap decreases mildly to being ~33% higher in the ashed samples.
d. TEM, STEM and APT demonstrated the platy morphology of discrete but often aggregated elongated crystals, and, in pristine samples, it revealed the presence of C (carbon) within the mineral crystal domains.
e. Quantitative X-ray crystallite size analysis (~35 nm long) showed that ashing at 550 °C for 10 hours did not lead to any appreciable grain growth or platelet elongation.

Acknowledgements

We thank Norbert Schell from HZG for help and we acknowledge DESY for the hydrostatic experiments and for access to beamtime on the HEMS P07 Beamline in PETRA III, Hamburg. APT and STEM analysis were performed at the National Institute for Materials Science, Tsukuba. Bright and dark field TEM imaging was performed at the Canadian Center for Electron Microscopy CCEM. Jean-Baptiste Forien acknowledges support by the US Dept. of Energy (contract No. DE-AC52-07NA27344).

References

[1] J.D. Currey, Bones: structure and mechanics, Princeton University Press, Princeton, NJ, USA, 2002.
[2] W.J. Landis, M.J. Song, A. Leith, L. McEwen, B.F. McEwen, Mineral and organic matrix interaction in normally calcifying tendon visualized in three dimensions by high-voltage electron microscopic tomography and graphic image reconstruction, J. Struct. Biol. 110 (1993) 39–54. https://doi.org/10.1006/jsbi.1993.1003.
[3] S. Weiner, W. Traub, Bone structure: from angstroms to microns, FASEB J. Off. Publ. Fed. Am. Soc. Exp. Biol. 6 (1992) 879–885.
[4] B. Langelier, X. Wang, K. Grandfield, Atomic scale chemical tomography of human bone, Sci. Rep. 7 (2017) 1–9. https://doi.org/10.1038/srep39958.
[5] E.A. McNally, H.P. Schwarcz, G.A. Botton, A.L. Arsenault, A model for the ultrastructure of bone based on electron microscopy of ion-milled sections, PLoS ONE. 7 (2012) e29258. https://doi.org/10.1371/journal.pone.0029258.
[6] S. Weiner, H.D. Wagner, The material bone: structure-mechanical function relations, Annu. Rev.

Mater. Sci. 28 (1998) 271–298.
[7] N. Reznikov, R. Shahar, S. Weiner, Bone hierarchical structure in three dimensions, Acta Biomater. (2014). https://doi.org/10.1016/j.actbio.2014.05.024.
[8] H.A. Lowenstam, S. Weiner, On Biomineralization, Oxford University Press, 1989. https://global.oup.com/academic/product/on-biomineralization-9780195049770?cc=us&lang=en& (accessed March 14, 2020).
[9] J. Seto, H.S. Gupta, P. Zaslansky, H.D. Wagner, P. Fratzl, Tough lessons from bone: extreme mechanical anisotropy at the mesoscale, Adv. Funct. Mater. 18 (2008) 1905–1911. https://doi.org/10.1002/adfm.200800214.
[10] J.D. Currey, K. Brear, P. Zioupos, Dependence of mechanical properties on fibre angle in narwhal tusk, a highly oriented biological composite, J. Biomech. 27 (1994) 885–897.
[11] J.-B. Forien, I. Zizak, C. Fleck, A. Petersen, P. Fratzl, E. Zolotoyabko, P. Zaslansky, Water-mediated collagen and mineral nanoparticle interactions guide functional deformation of human tooth dentin., Chem. Mater. 28 (2016) 3416–3427. https://doi.org/10.1021/acs.chemmater.6b00811.
[12] J.-B. Forien, C. Fleck, P. Cloetens, G. Duda, P. Fratzl, E. Zolotoyabko, P. Zaslansky, Compressive Residual Strains in Mineral Nanoparticles as a Possible Origin of Enhanced Crack Resistance in Human Tooth Dentin, Nano Lett. 15 (2015) 3729–3734. https://doi.org/10.1021/acs.nanolett.5b00143.
[13] Y. Liu, R. Ballarini, S.J. Eppell, Tension tests on mammalian collagen fibrils, Interface Focus. 6 (2016). https://doi.org/10.1098/rsfs.2015.0080.
[14] J.A.J. van der Rijt, K.O. van der Werf, M.L. Bennink, P.J. Dijkstra, J. Feijen, Micromechanical Testing of Individual Collagen Fibrils, Macromol. Biosci. 6 (2006) 697–702. https://doi.org/10.1002/mabi.200600063.
[15] Z.L. Shen, M.R. Dodge, H. Kahn, R. Ballarini, S.J. Eppell, Stress-Strain Experiments on Individual Collagen Fibrils, Biophys. J. 95 (2008) 3956–3963. https://doi.org/10.1529/biophysj.107.124602.
[16] F. Hang, A.H. Barber, Nano-mechanical properties of individual mineralized collagen fibrils from bone tissue, J. R. Soc. Interface. 8 (2011) 500–505. https://doi.org/10.1098/rsif.2010.0413.
[17] H.J. Gao, B.H. Ji, I.L. Jager, E. Arzt, P. Fratzl, Materials become insensitive to flaws at nanoscale: lessons from nature, Proc. Natl. Acad. Sci. 100 (2003) 5597–5600. https://doi.org/10.1073/pnas.0631609100.
[18] H.S. Gupta, J. Seto, W. Wagermaier, P. Zaslansky, P. Boesecke, P. Fratzl, Cooperative deformation of mineral and collagen in bone at the nanoscale, Proc. Natl. Acad. Sci. 103 (2006) 17741–17746.
[19] R.Z. LeGeros, Apatites in biological systems, Prog. Cryst. Growth Charact. 4 (1981) 1–45. https://doi.org/10.1016/0146-3535(81)90046-0.
[20] J. Bhimasenachar, Elastic constants of apatite., Proc. Indian Acad. Sci. A22 (1945) 209–214.
[21] M.C. Sha, Z. Li, R.C. Bradt, Single-crystal elastic constants of fluorapatite, Ca5F (PO4)3, J. Appl. Phys. 75 (1994) 7784–7787. https://doi.org/10.1063/1.357030.
[22] S. a. M. Tofail, D. Haverty, F. Cox, J. Erhart, P. Hána, V. Ryzhenko, Direct and ultrasonic measurements of macroscopic piezoelectricity in sintered hydroxyapatite, J. Appl. Phys. 105 (2009) 064103. https://doi.org/10.1063/1.3093863.
[23] H.S. Yoon, R.E. Newham, Elastic properties of fluorapatite, Am. Mineral. 54 (1969) 1193–1197.
[24] R.S. Gilmore, J.L. Katz, Elastic properties of apatites, J. Mater. Sci. 17 (1982) 1131–1141. https://doi.org/10.1007/BF00543533.
[25] J.L. Katz, K. Ukraincik, On the anisotropic elastic properties of hydroxyapatite, J. Biomech. 4 (1971) 221–227. https://doi.org/10.1016/0021-9290(71)90007-8.
[26] F. Brunet, D.R. Allan, S.A.T. Redfern, R.J. Angel, R. Miletich, H.J. Reichmann, J. Sergent, M. Hanfland, Compressibility and thermal expansivity of synthetic apatites, Ca 5 (PO 4) 3 X with X = OH, F and Cl, Eur. J. Mineral. 11 (1999) 1023–1035.

[27] P. Comodi, Y. Liu, P.F. Zanazzi, M. Montagnoli, Structural and vibrational behaviour of fluorapatite with pressure. Part I: in situ single-crystal X-ray diffraction investigation, Phys. Chem. Miner. 28 (2001) 219–224. https://doi.org/10.1007/s002690100154.
[28] X. Liu, S.R. Shieh, M.E. Fleet, L. Zhang, Q. He, Equation of state of carbonated hydroxylapatite at ambient temperature up to 10 GPa: Significance of carbonate, Am. Mineral. 96 (2011) 74–80. https://doi.org/10.2138/am.2011.3535.
[29] K.N. Matsukage, S. Ono, T. Kawamoto, T. Kikegawa, The compressibility of a natural apatite, Phys. Chem. Miner. 31 (2004) 580–584. https://doi.org/10.1007/s00269-004-0415-x.
[30] K. Teraoka, A. Ito, K. Maekawa, K. Onuma, T. Tateishi, S. Tsutsumi, Mechanical properties of hydroxyapatite and OH-carbonated hydroxyapatite single crystals, J. Dent. Res. 77 (1998) 1560–1568. https://doi.org/10.1177/00220345980770071201.
[31] S.F. Ang, E.L. Bortel, M.V. Swain, A. Klocke, G.A. Schneider, Size-dependent elastic/inelastic behavior of enamel over millimeter and nanometer length scales, Biomaterials. 31 (2010) 1955–1963. https://doi.org/10.1016/j.biomaterials.2009.11.045.
[32] L. Angker, C. Nockolds, M.V. Swain, N. Kilpatrick, Correlating the mechanical properties to the mineral content of carious dentine—a comparative study using an ultra-micro indentation system (UMIS) and SEM-BSE signals, Arch. Oral Biol. 49 (2004) 369–378. https://doi.org/10.1016/j.archoralbio.2003.12.005.
[33] R.G. Craig, F.A. Peyton, D.W. Johnson, Compressive properties of enamel, dental cements, and gold, J. Dent. Res. 40 (1961) 936–945. https://doi.org/10.1177/00220345610400051901.
[34] S. Habelitz, S.J. Marshall, G.W. Marshall Jr, M. Balooch, Mechanical properties of human dental enamel on the nanometre scale, Arch. Oral Biol. 46 (2001) 173–183. https://doi.org/10.1016/S0003-9969(00)00089-3.
[35] R. Snyders, D. Music, D. Sigumonrong, B. Schelnberger, J. Jensen, J.M. Schneider, Experimental and ab initio study of the mechanical properties of hydroxyapatite, Appl. Phys. Lett. 90 (2007) 193902. https://doi.org/10.1063/1.2738386.
[36] B. Viswanath, R. Raghavan, U. Ramamurty, N. Ravishankar, Mechanical properties and anisotropy in hydroxyapatite single crystals, Scr. Mater. 57 (2007) 361–364. https://doi.org/10.1016/j.scriptamat.2007.04.027.
[37] H.H.K. Xu, D.T. Smith, S. Jahanmir, E. Romberg, J.R. Kelly, V.P. Thompson, E.D. Rekow, Indentation damage and mechanical properties of human enamel and dentin, J. Dent. Res. 77 (1998) 472–480. https://doi.org/10.1177/00220345980770030601.
[38] E.D. Yilmaz, H. Jelitto, G.A. Schneider, Uniaxial compressive behavior of micro-pillars of dental enamel characterized in multiple directions, Acta Biomater. 16 (2015) 187–195. https://doi.org/10.1016/j.actbio.2015.01.015.
[39] A.C. Deymier, A.K. Nair, B. Depalle, Z. Qin, K. Arcot, C. Drouet, C.H. Yoder, M.J. Buehler, S. Thomopoulos, G.M. Genin, J.D. Pasteris, Protein-free formation of bone-like apatite: New insights into the key role of carbonation, Biomaterials. 127 (2017) 75–88. https://doi.org/10.1016/j.biomaterials.2017.02.029.
[40] E. Menéndez-Proupin, S. Cervantes-Rodríguez, R. Osorio-Pulgar, M. Franco-Cisterna, H. Camacho-Montes, M.E. Fuentes, Computer simulation of elastic constants of hydroxyapatite and fluorapatite, J. Mech. Behav. Biomed. Mater. 4 (2011) 1011–1020. https://doi.org/10.1016/j.jmbbm.2011.03.001.
[41] N.Y. Mostafa, P.W. Brown, Computer simulation of stoichiometric hydroxyapatite: Structure and substitutions, J. Phys. Chem. Solids. 68 (2007) 431–437. https://doi.org/10.1016/j.jpcs.2006.12.011.
[42] W.Y. Ching, P. Rulis, A. Misra, Ab initio elastic properties and tensile strength of crystalline hydroxyapatite, Acta Biomater. 5 (2009) 3067–3075. https://doi.org/10.1016/j.actbio.2009.04.030.

[43] T. Sui, M.A. Sandholzer, N. Baimpas, I.P. Dolbnya, G. Landini, A.M. Korsunsky, Hierarchical modelling of elastic behaviour of human enamel based on synchrotron diffraction characterisation, J. Struct. Biol. 184 (2013) 136–146. https://doi.org/10.1016/j.jsb.2013.09.023.
[44] G. Ulian, G. Valdrè, Second-order elastic constants of hexagonal hydroxylapatite ($P6_3$) from *ab initio* quantum mechanics: Comparison between DFT functionals and basis sets, Int. J. Quantum Chem. 118 (2018) e25500. https://doi.org/10.1002/qua.25500.
[45] H. Yao, L. Ouyang, W.-Y. Ching, Ab initio calculation of elastic constants of ceramic crystals, J. Am. Ceram. Soc. 90 (2007) 3194–3204. https://doi.org/10.1111/j.1551-2916.2007.01931.x.
[46] S.S. Bhat, U.V. Waghmare, U. Ramamurty, First-principles study of structure, vibrational, and elastic properties of stoichiometric and calcium-deficient hydroxyapatite, Cryst. Growth Des. 14 (2014) 3131–3141. https://doi.org/10.1021/cg5004269.
[47] C.-X. Li, Y.-H. Duan, W.-C. Hu, Electronic structure, elastic anisotropy, thermal conductivity and optical properties of calcium apatite Ca5(PO4)3X (X = F, Cl or Br), J. Alloys Compd. 619 (2015) 66–77. https://doi.org/10.1016/j.jallcom.2014.09.022.
[48] A. Slepko, A.A. Demkov, First-principles study of the biomineral hydroxyapatite, Phys. Rev. B. 84 (2011) 134108. https://doi.org/10.1103/PhysRevB.84.134108.
[49] J.-B. Forien, C. Fleck, C. Krywka, E. Zolotoyabko, P. Zaslansky, In situ compressibility of carbonated hydroxyapatite in tooth dentine measured under hydrostatic pressure by high energy X-ray diffraction, J. Mech. Behav. Biomed. Mater. 50 (2015) 171–179. https://doi.org/10.1016/j.jmbbm.2015.06.005.
[50] G. Daculsi, J.M. Bouler, R.Z. LeGeros, Adaptive crystal formation in normal and pathological calcifications in synthetic calcium phosphate and related biomaterials, Int. Rev. Cytol. 172 (1997) 129–191. https://doi.org/10.1016/s0074-7696(08)62360-8.
[51] J. de D. Teruel, A. Alcolea, A. Hernández, A.J.O. Ruiz, Comparison of chemical composition of enamel and dentine in human, bovine, porcine and ovine teeth, Arch. Oral Biol. 60 (2015) 768–775. https://doi.org/10.1016/j.archoralbio.2015.01.014.
[52] R.Z. LeGeros, O.R. Trautz, E. Klein, J.P. LeGeros, Two types of carbonate substitution in the apatite structure, Experientia. 25 (1969) 5–7. https://doi.org/10.1007/BF01903856.
[53] M.E. Fleet, Infrared spectra of carbonate apatites: Evidence for a connection between bone mineral and body fluids, Am. Mineral. 102 (2017) 149–157. https://doi.org/10.2138/am-2017-5704.
[54] A.J. Ortiz-Ruiz, J. de D. Teruel-Fernández, L.A. Alcolea-Rubio, A. Hernández-Fernández, Y. Martínez-Beneyto, F. Gispert-Guirado, Structural differences in enamel and dentin in human, bovine, porcine, and ovine teeth, Ann. Anat. Anat. Anz. Off. Organ Anat. Ges. 218 (2018) 7–17. https://doi.org/10.1016/j.aanat.2017.12.012.
[55] P. Grøn, M. Spinelli, O. Trautz, F. Brudevold, The effect of carbonate on the solubility of hydroxylapatite, Arch. Oral Biol. 8 (1963) 251–263. https://doi.org/10.1016/0003-9969(63)90016-5.
[56] J.J. Lim, A.R. Liboff, Thermogravimetric Analysis of Dentin, J. Dent. Res. 51 (1972) 509–514. https://doi.org/10.1177/00220345720510024401.
[57] L.D. Mkukuma, J.M.S. Skakle, I.R. Gibson, C.T. Imrie, R.M. Aspden, D.W.L. Hukins, Effect of the proportion of organic material in bone on thermal decomposition of bone mineral: an investigation of a variety of bones from different species using thermogravimetric analysis coupled to mass spectrometry, high-temperature X-ray diffraction, and fourier transform infrared spectroscopy, Calcif. Tissue Int. 75 (2004) 321–328. https://doi.org/10.1007/s00223-004-0199-5.
[58] T.J.U. Thompson, M. Gauthier, M. Islam, The application of a new method of Fourier Transform Infrared Spectroscopy to the analysis of burned bone, J. Archaeol. Sci. 36 (2009) 910–914. https://doi.org/10.1016/j.jas.2008.11.013.

[59] M. Greiner, A. Rodríguez-Navarro, M.F. Heinig, K. Mayer, B. Kocsis, A. Göhring, A. Toncala, G. Grupe, W.W. Schmahl, Bone incineration: An experimental study on mineral structure, colour and crystalline state, J. Archaeol. Sci. Rep. 25 (2019) 507–518. https://doi.org/10.1016/j.jasrep.2019.05.009.
[60] J. Reyes-Gasga, R. García-García, M.J. Arellano-Jiménez, E. Sanchez-Pastenes, G.E. Tiznado-Orozco, I.M. Gil-Chavarria, G. Gómez-Gasga, Structural and thermal behaviour of human tooth and three synthetic hydroxyapatites from 20 to 600°C, J. Phys. Appl. Phys. 41 (2008) 225407. https://doi.org/10.1088/0022-3727/41/22/225407.
[61] P. Shipman, G. Foster, M. Schoeninger, Burnt bones and teeth: an experimental study of color, morphology, crystal structure and shrinkage, J. Archaeol. Sci. 11 (1984) 307–325. https://doi.org/10.1016/0305-4403(84)90013-X.
[62] C. Krywka, I. Krasnov, R. Figuli, M. Burghammer, M. Müller, Determination of silkworm silk fibroin compressibility using high hydrostatic pressure with in situ x-ray microdiffraction, Macromolecules. 47 (2014) 7187–7193. https://doi.org/10.1021/ma501880h.
[63] C. Krywka, C. Sternemann, M. Paulus, M. Tolan, C. Royer, R. Winter, Effect of osmolytes on pressure-induced unfolding of proteins: a high-pressure SAXS study, ChemPhysChem. 9 (2008) 2809–2815. https://doi.org/10.1002/cphc.200800522.
[64] W. De Nolf, F. Vanmeert, K. Janssens, XRDUA: crystalline phase distribution maps by two-dimensional scanning and tomographic (micro) X-ray powder diffraction, J. Appl. Crystallogr. 47 (2014) 1107–1117. https://doi.org/10.1107/S1600576714008218.
[65] G. van Rossum, Python Tutorial, Centrum voor Wiskunde en Informatica, 1995.
[66] M. Newville, T. Stensitzki, D.B. Allen, M. Rawlik, A. Ingargiola, A. Nelson, Lmfit: non-linear least-square minimization and curve-fitting for python, Astrophys. Source Code Libr. (2016) ascl:1606.014.
[67] J.F. Nye, Physical Properties of Crystals: Their Representation by Tensors and Matrices, Édition : Reprint, Oxford University Press, Oxford Oxfordshire : New York, 1985.
[68] D. Tromans, Elastic anisotropy of HCP metal crystals and polycrystals, Int. J. Res. Rev. Appl. Sci. 6 (2011) 462–483.
[69] E. Zolotoyabko, Basic concepts of crystallography, Wiley-VCH, Weinheim, Germany, 2011.
[70] H.P. Schwarcz, D.M. Binkley, L. Luo, K. Grandfield, A search for apatite crystals in the gap zone of collagen fibrils in bone using dark-field illumination, Bone. 135 (2020) 115304. https://doi.org/10.1016/j.bone.2020.115304.
[71] H.P. Schwarcz, E.A. McNally, G.A. Botton, Dark-field transmission electron microscopy of cortical bone reveals details of extrafibrillar crystals, J. Struct. Biol. 188 (2014) 240–248. https://doi.org/10.1016/j.jsb.2014.10.005.
[72] J. Schindelin, I. Arganda-Carreras, E. Frise, V. Kaynig, M. Longair, T. Pietzsch, S. Preibisch, C. Rueden, S. Saalfeld, B. Schmid, J.-Y. Tinevez, D.J. White, V. Hartenstein, K. Eliceiri, P. Tomancak, A. Cardona, Fiji: an open-source platform for biological-image analysis, Nat. Methods. 9 (2012) 676–682. https://doi.org/10.1038/nmeth.2019.
[73] H.P. Schwarcz, The ultrastructure of bone as revealed in electron microscopy of ion-milled sections, Semin. Cell Dev. Biol. 46 (2015) 44–50. https://doi.org/10.1016/j.semcdb.2015.06.008.
[74] P.-Y. Chen, D. Toroian, P.A. Price, J. McKittrick, Minerals form a continuum phase in mature cancellous bone, Calcif. Tissue Int. 88 (2011) 351–361. https://doi.org/10.1007/s00223-011-9462-8.
[75] K. Grandfield, V. Vuong, H.P. Schwarcz, Ultrastructure of bone: hierarchical features from nanometer to micrometer scale revealed in focused ion beam sections in the TEM, Calcif. Tissue Int. 103 (2018) 606–616. https://doi.org/10.1007/s00223-018-0454-9.
[76] V. Jantou-Morris, M.A. Horton, D.W. McComb, The nano-morphological relationships between

apatite crystals and collagen fibrils in ivory dentine, Biomaterials. 31 (2010) 5275–5286. https://doi.org/10.1016/j.biomaterials.2010.03.025.
[77] T. Sui, M.A. Sandholzer, A.J.G. Lunt, N. Baimpas, A. Smith, G. Landini, A.M. Korsunsky, In situ X-ray scattering evaluation of heat-induced ultrastructural changes in dental tissues and synthetic hydroxyapatite, J. R. Soc. Interface. 11 (2014) 20130928. https://doi.org/10.1098/rsif.2013.0928.
[78] Z. Zyman, D. Rokhmistrov, I. Ivanov, M. Epple, The influence of foreign ions on the crystal lattice of hydroxyapatite upon heating, Mater. Werkst. 37 (2006) 530–532. https://doi.org/10.1002/mawe.200600032.
[79] P. Fratzl, H. Gupta, O. Paris, A. Valenta, P. Roschger, K. Klaushofer, Diffracting “stacks of cards” - some thoughts about small-angle scattering from bone, in: Scatt. Methods Prop. Polym. Mater., Springer Berlin / Heidelberg, 2005: pp. 273–291. http://www.springerlink.com/content/rcg999gnuhrx234u/abstract/ (accessed May 8, 2012).
[80] N. Reznikov, M. Bilton, L. Lari, M.M. Stevens, R. Kröger, Fractal-like hierarchical organization of bone begins at the nanoscale, Science. 360 (2018). https://doi.org/10.1126/science.aao2189.
[81] J.D. Pasteris, B. Wopenka, J.J. Freeman, K. Rogers, E. Valsami-Jones, J.A.M. van der Houwen, M.J. Silva, Lack of OH in nanocrystalline apatite as a function of degree of atomic order: implications for bone and biomaterials, Biomaterials. 25 (2004) 229–238. https://doi.org/10.1016/S0142-9612(03)00487-3.
[82] R.Z. Zapanta-LeGeros, Effect of carbonate on the lattice parameters of apatite, Nature. 206 (1965) 403–404. https://doi.org/10.1038/206403a0.
[83] H. Ou-Yang, E.P. Paschalis, W.E. Mayo, A.L. Boskey, R. Mendelsohn, Infrared microscopic imaging of bone: spatial distribution of CO3(2-), J. Bone Miner. Res. Off. J. Am. Soc. Bone Miner. Res. 16 (2001) 893–900. https://doi.org/10.1359/jbmr.2001.16.5.893.
[84] J.C. Elliott, Calcium Phosphate Biominerals, Rev. Mineral. Geochem. 48 (2002) 427–453. https://doi.org/10.2138/rmg.2002.48.11.
[85] S.L. Rowles, Chemistry of the mineral phase of dentine, in: Struct. Chem. Organ. Teeth, Miles, A.E.W., Academic Press, New York, 1967: pp. 201–246.
[86] C.A. Schneider, W.S. Rasband, K.W. Eliceiri, NIH Image to ImageJ: 25 years of image analysis, Nat. Methods. 9 (2012) 671–675. https://doi.org/10.1038/nmeth.2089.
[87] C. MessaoudiI, T. Boudier, C.O.S. Sorzano, S. Marco, TomoJ: tomography software for three-dimensional reconstruction in transmission electron microscopy, BMC Bioinformatics. 8 (2007) 288. https://doi.org/10.1186/1471-2105-8-288.